IEEE Access
Multidisciplinary | Rapid Review | Open Access Journal

Received July 1, 2020, accepted August 13, 2020, date of publication August 21, 2020, date of current version September 1, 2020.

Digital Object Identifier 10.1109/ACCESS.2020.3018471

Three-Impulse Return Orbit Design and Characteristic Analysis for Manned Lunar Missions

LIN LU AND HAIYANG LI
College of Aerospace Science and Engineering, National University of Defense Technology, Changsha 410073, China
Corresponding author: Haiyang Li (lihaiyang@nudt.edu.cn)

This work was supported in part by the National Natural Science Foundation of China under Grant 11372345.

ABSTRACT Return orbit design and characteristic analysis are very important issues in manned lunar missions. In this paper, a three-impulse return orbit scheme is studied. First, a convenient method based on the conical surface of the hyperbolic excess velocity is proposed, which can effectively perform an approximate analysis of the velocity increment characteristic. Second, a serial orbit design strategy is presented to determine the entire return orbit from the lunar parking orbit to the intended landing site. In the initial design, a three-segment orbit patched method based on the pseudo-perilune parameters is applied. Backward and forward calculations are conducted in the hybrid orbit model and the patched-conic model respectively, with the perilune of the lunar escape orbit as the dividing point. In the accurate design, a two-segment orbit patched method is employed in the high-fidelity model. Finally, numerical simulations are used to verify the effectiveness and feasibility of the orbit design strategy. According to many simulation results achieved by this strategy, the characteristics of fixed-point return window and velocity increment are further analyzed.

INDEX TERMS Manned lunar mission, return orbit, conical surface of the hyperbolic excess velocity, pseudo-perilune parameters, orbit characteristic analysis.

I. INTRODUCTION

Many countries are focusing on manned deep space exploration, and the moon is regarded as the next goal [1]. The White House has recently demanded that the National Aeronautics and Space Administration (NASA) send people back to the lunar surface by 2024 [2]. Russia is expected to complete its first manned lunar landing in 2031 and begin the establishment of the first lunar base [3]. The European Space Agency (ESA) has repeatedly proposed the idea of building a ''lunar village'' [4]. The Japanese government has clearly stated that Japan has joined the American ''Gateway'' project [5]. With the success of the ''Chang'E-4'' mission [6], [7], increasingly people are also looking forward to realizing a Chinese manned lunar landing as soon as possible [8]. The lunar landing areas of the early American Apollo missions were mainly concentrated near the lunar equator. Due to the special environment of the lunar polar region and the discovery of water ice [9], [10], the lunar polar region has irreplaceable value for scientific exploration and application development. Therefore, humans are paying increasing attention to the lunar high-latitude region and taking it as a hot spot [11], [12], even considering the establishment of a lunar base in the lunar polar region in the future. Manned lunar missions are large systematic projects, of which the orbit scheme is an important component. The design and characteristic analysis of the orbit are of great significance to the mission. As one of the requirements of the manned lunar landing, the spacecraft must have the capability to safely return to the intended landing site from any lunar parking orbit at any time in case the mission fails and must be aborted.

Many scholars have conducted research on the design and analysis of the lunar return orbit scheme. Wooster proposed three orbit schemes of moon-to-Earth transfer and compared the relationship between the velocity increment required by different orbit schemes and the angle of orbit plane change [13]. Jones and Ocampo used nonlinear programming algorithms to optimize impulsive escape orbits from a circumlunar orbit to a given hyperbolic excess velocity vector and compared single-impulse and three-impulse maneuver schemes [14]. Wang *et al.* introduced an optimization design procedure for a two-impulse maneuver scheme based on a single-impulse maneuver scheme and discussed different schemes [15]. Ocampo and Saudemont

The associate editor coordinating the review of this manuscript and approving it for publication was Fabrizio Messina.

developed an analytical procedure to generate an initial feasible solution of the multi-maneuver moon-to-Earth orbit based on the two-body model by adopting the differential correction algorithm [16]. Li *et al.* derived an analytical design method for determining the moon-to-Earth orbit of a single-impulse maneuver to support the lunar exploration requirement of anytime return [17]. Edelbaum presented an approximate analytical model to achieve minimum impulse transfer between a given circumlunar orbit and a given hyperbolic velocity vector by fixing the transfer time between the first and last impulses [18]. Zheng and Zhou provided a search strategy of the return window for moon-to-Earth orbits [19]. Gavrikova and Golubey applied the Lambert algorithm to solve the problem of three-impulse return orbit from the lunar parking orbit in the three-body problem model [20]. Park *et al.* investigated the fuel-optimal moon-to-Earth orbit design in the restricted four-body problem. A nonlinear constrained fuel-optimal control problem was formulated and solved by using the Legendre pseudospectral method [21]. Liu *et al.* studied a three-impulse orbit control strategy based on the elliptical four-body model, which could effectively guarantee the re-entry point accuracy of the low energy return orbit, but was unsuitable for the manned return missions [22]. Shen *et al.* adopted the multi-start algorithm to optimize the single-impulse return orbit and analyzed the orbit characteristics such as the selenocentric orbit parameters, the geocentric orbit parameters and the velocity increment [23]. He *et al.* established a mathematical model for finding the landing window and designing the return orbit for the manned lunar missions, and investigated the coupling mechanism from the spatial geometric relationship [24]. Some scholars have also performed studies on the return orbit for lunar polar exploration missions. Some orbit schemes for a lunar South Pole Aitken basin sample return mission have been proposed [25], [26]. Feng and Zhang outlined a return window search strategy departing from the lunar polar orbit considering various constraints and an improved multi-conic method was devoted to the generation of initial return orbits [27].

It can be concluded that the previous studies have the following limitations: First, the analytical models proposed by some scholars can provide good initial values for high-fidelity optimization, but as preliminary analysis tools for orbit characteristics, they appear that the derivation processes are complex. Second, many scholars adopted the traditional patched-conic method to design the initial fixed-point return orbit, which takes the orbit parameters of the outbound point of the lunar sphere of influence as the design variables and computes the geocentric return orbit parameters by iteration. This case tends to result in more errors.

The objective of our research is to overcome the above shortcomings. The main contributions of this paper are summarized as follows. We propose the conical surface of the hyperbolic excess velocity and establish a convenient model as a preliminary analysis tool for the velocity increment characteristic analysis of three-impulse return orbit. We also present a serial design strategy to determine and optimize the entire three-impulse return orbit considering the constraint of the landing point location. The method proposed in the initial design takes the departure parameters as the design variables and performs forward calculation in the lunar escape segment without iteration. In addition, we analyze the fixed-point return window characteristic and velocity increment characteristic by this design strategy.

This paper is structured in six sections, including this introductory section. The second section begins by presenting a return orbit scheme of the three-impulse maneuver. In the third section, a model is established to preliminarily analyze the velocity increment characteristic. The fourth section describes a serial solution strategy applied to design the entire return orbit. In the initial design, a three-segment orbit patched method based on the pseudo-perilune parameters is used. In the accurate design, the two-segment orbit patched method is constructed in the high-fidelity model. The fifth section is devoted to extensive numerical simulations, in which the validity and feasibility of the orbit design strategy are examined. Further detailed analysis of orbit characteristics is demonstrated based on a large amount of simulation results by this strategy. This paper ends with the sixth section which briefly summarizes the conclusions and implications on this topic.

II. RETURN ORBIT SCHEME OF THREE-IMPULSE MANEUVER

When manned lunar missions are intended for lunar high-latitude regions, the characteristic of the lunar parking orbit is significant. In this case, the return orbit starting from the lunar parking orbit has a higher requirement for the spacecraft's return capability. Since it is difficult to adopt the conventional return orbit scheme of the tangential single-impulse maneuver, performing an out-of-plane orbit change is necessary [28]. Methods for out-of-plane orbit change generally include the single-impulse maneuver and the three-impulse maneuver [29]. When the angle of the orbit plane to be adjusted is large, the velocity increment required for the single-impulse maneuver is excessive [30], which is difficult to achieve in engineering practice. However, the three-impulse maneuver can effectively reduce the velocity increment for adjusting the orbit plane, especially when the angle of the orbit plane adjustment is large. It can be known that the three-impulse maneuver method is more suitable for the design of the return orbit scheme for lunar high-latitude region missions.

According to the above analysis, this paper proposes a return orbit scheme of a three-impulse maneuver. The specific process is described as follows: as shown in Fig. 1, first, the spacecraft enters the first large elliptical transition orbit (ETO1) by applying the first impulse in the tangential direction of point A of the lunar polar orbit (LPO). The second impulse is applied at point B of ETO1 to adjust the orbit plane into the second large elliptical transition orbit (ETO2). The position of point B is determined by the intersection of the LPO plane and the ETO2 plane, and the point of intersection

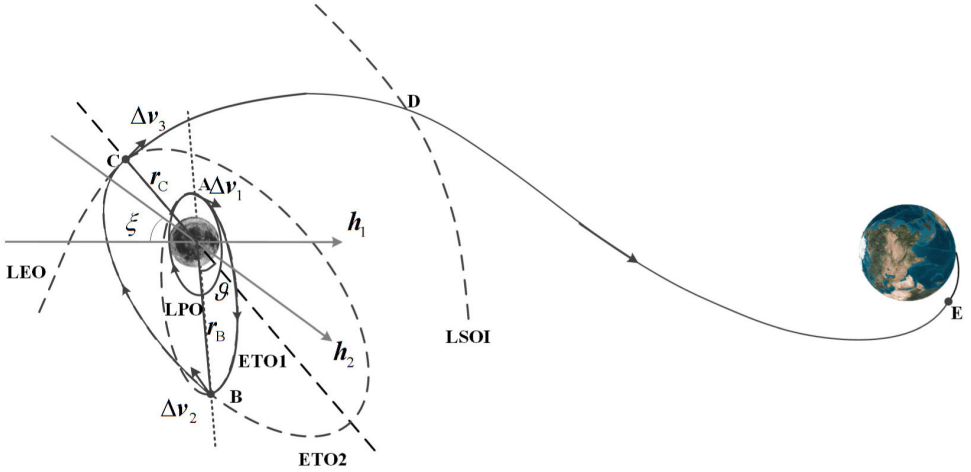

FIGURE 1. Return orbit scheme of three-impulse maneuver.

that is closer to the apolune of ETO2 is selected. Finally, the spacecraft enters the lunar escape orbit (LEO) by applying the third impulse in the tangential direction of point C, which is the perilune of ETO2.

III. METHOD FOR THE PRELIMINARY ANALYSIS OF VELOCITY INCREMENT CHARACTERISTIC

For the return orbit scheme of the three-impulse maneuver, this section presents a convenient method for the preliminary analysis of the velocity increment characteristic, regardless of the Earth's terminal constraints. Based on the conical surface of the hyperbolic excess velocity, this method can effectively perform an approximate analysis of the velocity increment required during the three-impulse maneuver by intuitively and succinctly utilizing the angular relationship of the related vectors in space.

A. CONICAL SURFACE OF THE HYPERBOLIC EXCESS VELOCITY

In the sphere of the influence model, the spacecraft's orbit in the lunar sphere of influence is a hyperbolic orbit. The velocity of the spacecraft at the boundary of the lunar sphere of influence can be regarded as the velocity in infinity, which is the excess velocity of the hyperbolic orbit. It can be expressed by the velocity and the distance from the centre of the moon of the spacecraft at the perilune of the hyperbolic orbit:

$$v_\infty = \sqrt{v_p^2 - \frac{2\mu_m}{r_p}} \tag{1}$$

where μ_m is the gravitational parameters of the moon, r_p is the distance of the perilune of the hyperbolic orbit from the centre of the moon, and v_p is the perilune velocity.

The magnitude of the velocity at the injection point of the lunar sphere of influence $\boldsymbol{v}_{\infty in}$ is the same as the magnitude of the velocity at the outbound point of the lunar sphere of influence $\boldsymbol{v}_{\infty out}$, and they can be considered as being along the direction of the asymptote. When $\boldsymbol{v}_{\infty in}$ and r_p are given, the distribution of all possible $\boldsymbol{v}_{\infty out}$ forms a conical surface

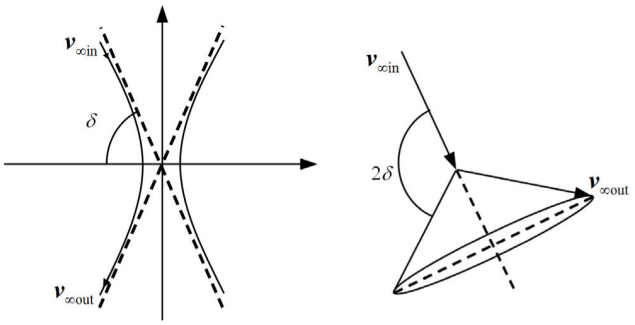

FIGURE 2. Conical surface of the hyperbolic excess velocity.

whose axis direction is along $\boldsymbol{v}_{\infty in}$. As shown in Fig. 2, the conical surface is defined as the conical surface of the hyperbolic excess velocity. The half-cone angle of the cone is $(\pi - 2\delta)$, where $\delta = \arccos\frac{1}{e}$, and e is the eccentricity of the hyperbolic orbit. The end points of all $\boldsymbol{v}_{\infty out}$ vectors constitute a circle with a radius of $v_\infty \sin(2\delta)$.

B. VELOCITY INCREMENT CALCULATION

The moon is the central celestial body. The normal unit vectors of the LPO plane and the LEO plane are denoted by $\boldsymbol{h}_1$ and $\boldsymbol{h}_2$, respectively. The position vectors at which the first impulse, the second impulse and the third impulse are applied are denoted by $\boldsymbol{r}_A, \boldsymbol{r}_B$ and $\boldsymbol{r}_C$, respectively. The angular relationship of the related vectors in space is given below. As shown in Fig. 3, when the target hyperbolic excess velocity vector $\boldsymbol{v}_{\infty out}$ is specified, the distribution of all possible $\boldsymbol{r}_C$ vectors forms a conical surface whose axis direction is along $\boldsymbol{v}_{\infty out}$. The half-cone angle of the cone is denoted by η. Taking the plane determined by $\boldsymbol{v}_{\infty out}$ and $\boldsymbol{h}_1$ as the reference plane, the rotation angle of $\boldsymbol{r}_C$ around $\boldsymbol{v}_{\infty out}$ is denoted by σ. When σ is determined, $\boldsymbol{r}_C$ can be determined accordingly and the LEO plane can be determined by $\boldsymbol{v}_{\infty out}$ and $\boldsymbol{r}_C$. In addition, when $\boldsymbol{r}_C$ is given, the distribution of all possible $\boldsymbol{r}_B$ vectors forms a conical surface with $\boldsymbol{r}_C$ along the axials direction, and the half-cone angle of the cone is denoted by α. The angle

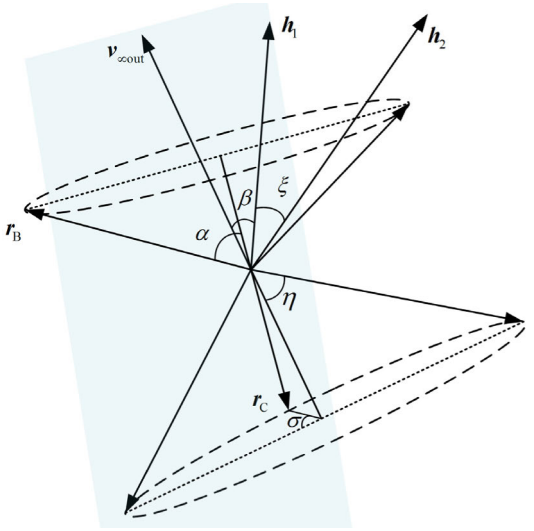

FIGURE 3. Illustration of the spatial geometric relationship.

between $\boldsymbol{h}_1$ and $\boldsymbol{v}_{\infty out}$ is denoted by β. The angle between the orbit planes of the LPO and the LEO is denoted by ξ, which is also the angle between $\boldsymbol{h}_1$ and $\boldsymbol{h}_2$.

According to the spatial geometric relationship, the following angular relationships can be obtained:

$$\sin(\frac{\pi}{2} - \xi) = \sin\beta \sin\sigma \tag{2}$$

$$\cos(\frac{\pi}{2} - \xi)\cos(\frac{\pi}{2} - \eta - \alpha) = \cos\beta \tag{3}$$

The calculation of the velocity increment during the three-impulse maneuver is performed below. The orbit period of ETO1 is denoted by T_{tra}, and the semi-major axis of ETO1 is expressed as

$$a_{tra} = (\frac{\mu_m}{4\pi^2} T_{tra}^2)^{\frac{1}{3}} \tag{4}$$

The velocity increment of the first maneuver can be computed by

$$\Delta v_1 = \sqrt{\mu_m(\frac{2}{r_A} - \frac{1}{a_{tra}})} - \sqrt{\frac{\mu_m}{r_A}} \tag{5}$$

The semi-major axis of LEO is

$$a_{LEO} = \frac{\mu_m}{v_{\infty out}^2} \tag{6}$$

In the preliminary analysis, assuming that the second impulse is used only to change the out-of-plane difference without adjusting the size of the transition orbit, the semi-major axis of ETO1 remains unchanged. The velocity increment of the third maneuver can be calculated by

$$\Delta v_3 = \sqrt{\mu_m(\frac{2}{r_C} + \frac{1}{a_{LEO}})} - \sqrt{\mu_m(\frac{2}{r_C} - \frac{1}{a_{tra}})} \tag{7}$$

The eccentricity of LEO e_{LEO} and the half-cone angle of cone η are given by

$$e_{LEO} = \frac{r_C}{a_{LEO}} + 1 \tag{8}$$

$$\eta = \arccos\frac{1}{e_{LEO}} \tag{9}$$

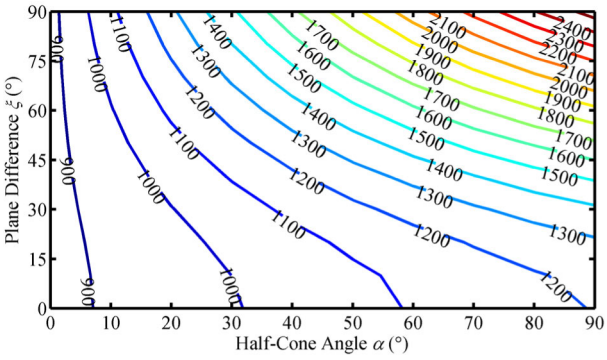

FIGURE 4. Total velocity increment versus plane difference ξ and half-cone angle α.

The velocity increment of the second maneuver can be obtained by the equation of the out-of-plane maneuver:

$$\Delta v_2 = 2v_{\tau 2}\sin\frac{\xi}{2} \tag{10}$$

where $v_{\tau 2}$ is the lateral velocity at $\boldsymbol{r}_B$ before the second impulse is applied, which can be expressed as

$$v_{\tau 2} = \frac{\mu_m}{h_{tra}}(1 + e_{tra}\cos f_B) = \frac{\mu_m}{h_{tra}}(1 - e_{tra}\cos\alpha) \tag{11}$$

where h_{tra} is the angular momentum of ETO1, e_{tra} is the eccentricity of ETO1, and f_B is the true anomaly at the point of ETO1 where the second impulse is applied.

When $\boldsymbol{v}_{\infty out}$ is specified, β and η are determined accordingly. α and ξ can be expressed in terms of σ by combining (2) and (3). Hence, Δv_2 can be expressed as a function with respect to σ.

The total velocity increment is expressed as

$$\Delta v = \Delta v_1 + \Delta v_2 + \Delta v_3 \tag{12}$$

C. EXAMPLES AND ANALYSIS

In this subsection, based on the above method, the velocity increment characteristic of the return orbit scheme of the three-impulse maneuver is analyzed with examples. The parameters of the example are set as follows by referring to the previous study [28]: the radius of LPO is 1938 km, the orbit period of ETO1 is 24 h, the magnitude of $\boldsymbol{v}_{\infty out}$ is 1000 m/s, and β is 45°. Fig. 4 shows that Δv is a function of ξ and α. It can be seen that Δv is greatly affected by ξ and α. The larger ξ is, the greater Δv is. The larger α is, the greater Δv is. Fig. 5 presents the variation of Δv versus σ. As indicated in the figure, Δv appears to decrease first and then increase with increasing σ. When σ is 51.7°, Δv reaches a minimum of 1119.91 m/s, while Δv reaches a maximum of 1271.30 m/s when σ is 90°.

The corresponding Δv is optimally calculated with different orbit periods of ETO T_{tra} and with the other parameters unchanged. The effect of T_{tra} on the total velocity increment is analyzed. The variation of Δv for the range in T_{tra} from 12 h to 48 h is shown in Fig. 6. A noticeable characteristic of the curve is that Δv decreases with increasing T_{tra}, but the extent of the change is not large, and the maximum and minimum values differ by

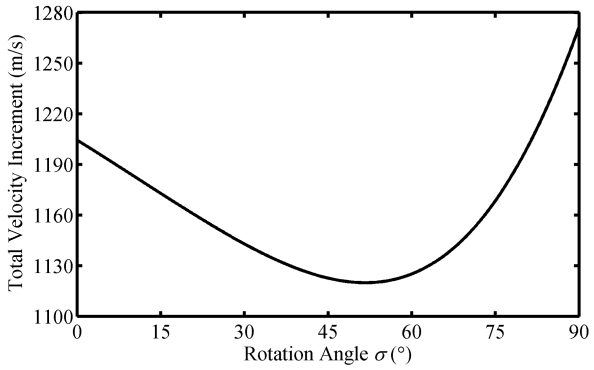

FIGURE 5. Total velocity increment versus rotation angle σ.

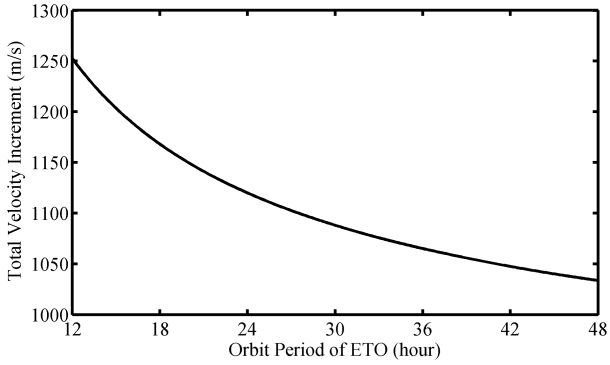

FIGURE 6. Total velocity increment versus orbit period of ETO.

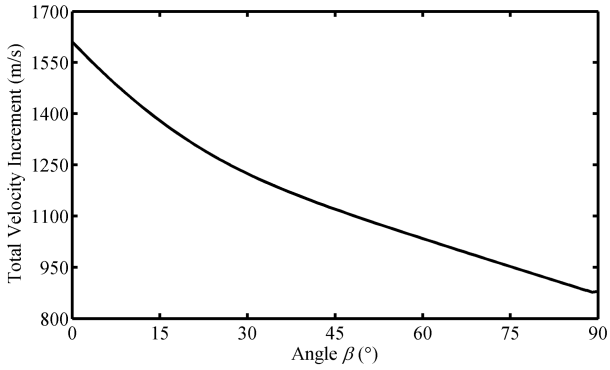

FIGURE 7. Total velocity increment versus angle β.

approximately 220 m/s. This characteristic is consistent with the conclusion obtained in [28].

The corresponding Δv is optimally calculated with different β and other parameters hold constant. As illustrated in Fig. 7, it is observed that as β gradually increases, Δv is gradually reduced, with a maximum of about 1600 m/s and a minimum of less than 900 m/s. This characteristic can be explained by the spatial geometric relationships of orbits. For example, when β is 90°, the plane of LPO coincides with the plane of LEO, which means that there is no need to adjust the orbit plane, so Δv is at its minimum.

The corresponding velocity increment is calculated with different magnitudes of $\boldsymbol{v}_{\infty \mathrm{out}}$ and other parameters held constant. As indicated by Fig. 8, with increasing the magnitude of $\boldsymbol{v}_{\infty \mathrm{out}}$, Δv_1 is unchanged, Δv_2 decreases, and Δv_3 increases.

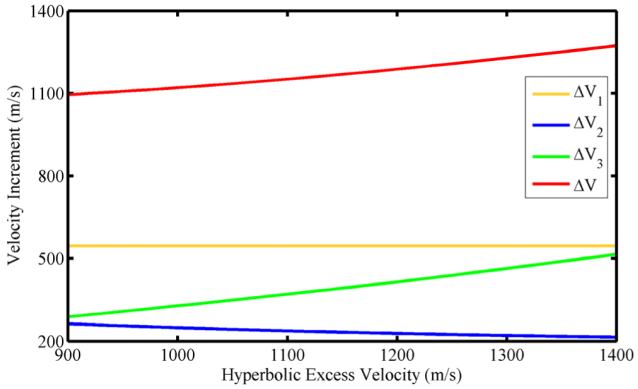

FIGURE 8. Velocity increment versus hyperbolic excess velocity.

In addition, Δv is plotted as a function of the magnitude of $\boldsymbol{v}_{\infty \mathrm{out}}$, which differs from the characteristics illustrated in Fig. 6 and Fig. 7. It is clear that Δv increases with increasing magnitude of $\boldsymbol{v}_{\infty \mathrm{out}}$. Thus, it is clear that the magnitude of $\boldsymbol{v}_{\infty \mathrm{out}}$ mainly influences Δv_3.

Some conclusions about the velocity increment characteristic can be drawn from the preliminary analysis. The total velocity increment of the return orbit scheme has a maximum of approximately 1600 m/s and a minimum of less than 900 m/s. Since the engineering specifications require the velocity increment of the return process to be reduced as much as possible, a smaller $\boldsymbol{v}_{\infty \mathrm{out}}$ can be selected to be targeted and the ETO with a longer period can be selected for the maneuver.

IV. ORBIT DESIGN STRATEGY

For the return orbit scheme of the three-impulse maneuver, this section proposes a serial solution strategy from the initial design to the accurate design to determine the entire return orbit, considering Earth's terminal constraints.

A. CONSTRAINT CONDITIONS

Compared with unmanned lunar missions, manned missions are more demanding in terms of the orbit design. Thus, the return orbit design for manned lunar missions should meet many complex constraints, including engineering and orbital constraints. The main engineering constraint is the flight time constraint. The flight time is restricted to ensure the safety of the astronauts in manned missions, so the orbit design must meet the following condition

$$T \leq T_{\max} \tag{13}$$

where $T_{\max}$ is the maximum flight time allowed for returning to Earth.

Orbital constraints mainly include the lunar parking orbit constraints, Earth's terminal constraints and the fixed-point return window constraint. The lunar parking orbit constraints comprise the orbit height, the right ascension of the ascending node and the orbit inclination:

$$\begin{cases} h_{\mathrm{A}} = h_{\mathrm{LPO}} \\ \Omega_{\mathrm{A}} = \Omega_{\mathrm{LPO}} \\ i_{\mathrm{A}} = i_{\mathrm{LPO}} \end{cases} \tag{14}$$

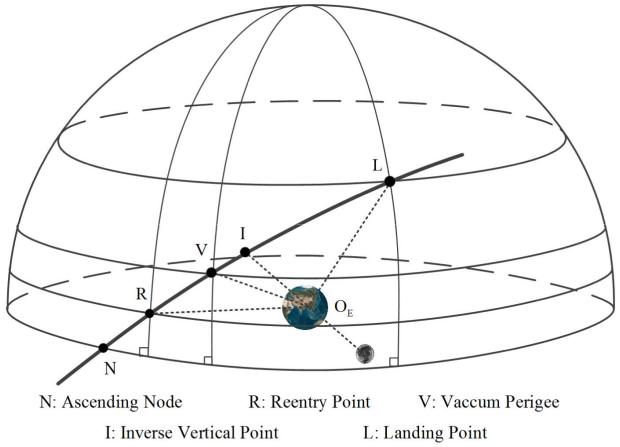

FIGURE 9. Feature point location of the terminal orbit.

where h_{LPO}, Ω_{LPO}, and i_{LPO} are the orbit height, the right ascension of the ascending node and the orbit inclination of the lunar polar orbit, respectively. i_{LPO} is equal to 90°.

To enable the spacecraft to return to the designated landing site, Earth's terminal constraints are primarily used to meet the requirements for the re-entry corridor and the location of the landing point:

$$\begin{cases} h_{ep} = h_{vcp} \\ i_E = i_{se} \\ \lambda_f = \lambda_{rp} \\ \phi_f = \phi_{rp} \end{cases} \tag{15}$$

where h_{vcp} is the altitude of the vacuum perigee which can be equivalent to the re-entry angle and the radius of the re-entry point [23]; i_{se} is the geocentric return orbit inclination; and λ_{rp} and ϕ_{rp} are the longitude and latitude of the re-entry point, respectively.

The longitude and latitude of the re-entry point can be obtained from the longitude and latitude of the landing point by the laws of spherical trigonometry. The positional relationship between the re-entry point and the landing point is shown in Fig. 9. The right ascension λ'_L and the declination ϕ'_L of the landing point can be computed by the given longitude and latitude of the landing point and the return time. The angle between the ascending node and re-entry point is expressed as

$$\psi_{NR} = \arcsin(\frac{\sin\phi'_L}{\sin i_{se}}) - \psi_{RL} \tag{16}$$

where ψ_{RL} is the range angle in the re-entry orbit phase.

The difference in the right ascension between the ascending node and the landing point is expressed as

$$\psi_{NL} = \arctan(\cos i_{se} \cdot \tan(\arcsin(\frac{\sin\phi'_L}{\sin i_{se}}))) \tag{17}$$

The right ascension λ'_{rp} and the declination ϕ'_{rp} of the re-entry point can be computed as

$$\lambda'_{rp} = \lambda'_L - \psi_{NL} + \arctan(\tan\psi_{NR}\cos i_{se}) \tag{18}$$

$$\phi'_{rp} = \arcsin(\sin\psi_{NR}\sin i_{se}) \tag{19}$$

Hence, the longitude and latitude of the re-entry point can be obtained.

The fixed-point return window constraint refers to the declination of the moon's inverse vertical point $-\phi'_m$ satisfying the condition of the fixed-point return at the return time:

$$\phi'_{vcp} < -\phi'_m < \phi'_L \tag{20}$$

where ϕ'_{vcp} is the declination of the vacuum perigee which can be obtained by laws of spherical trigonometry:

$$\phi'_{vcp} = \arcsin(\sin(\psi_{NR} + \psi_{RV})\sin i_{se}) \tag{21}$$

where ψ_{RV} is the angle between the re-entry point and the vacuum perigee, which can be calculated by the following nonlinear equation:

$$\tan\gamma = \frac{-e_{se}\sin\psi_{RV}}{1 + e_{se}\cos\psi_{RV}} \tag{22}$$

where γ is the re-entry angle and e_{se} is the eccentricity of the geocentric return orbit.

B. INITIAL DESIGN

In the initial design, a three-segment orbit patched method based on the pseudo-perilune parameters is proposed, which can improve the overall efficiency of the orbit design by decoupling the three-impulse maneuver and the lunar escape. The entire return process is divided into three segments, which are shown in Fig. 1: the three-impulse maneuver segment from departure point A to the perilune C of LEO, the selenocentric escape segment from point C to outbound point D of the lunar sphere of influence, and the geocentric return segment from point D to re-entry point E. Four orbit elements at point C are selected as design variables: the pseudo selenocentric longitude λ_{prl}, the pseudo selenocentric latitude φ_{prl}, the velocity azimuth angle i_{prl} and the selenocentric orbit eccentricity e_{prl} [31]. When the perilune time t_{prl} and the orbit height h_{prl} at point C are specified, the whole return orbit can be determined immediately by a set of pseudo-perilune parameters (λ_{prl}, φ_{prl}, i_{prl}, e_{prl}). The first segment is generated in a backward hybrid orbit model, while the forward patched-conic model is adopted to calculate the second and third segments.

1) BACKWARD HYBRID ORBIT MODEL

The duration of three-impulse maneuver segment is long, and it is difficult for the high-fidelity solution to converge quickly by employing the two-body model for the initial calculation. Thus, a backward hybrid orbit model that combines the two-body model with the high-fidelity orbit extrapolation model is introduced to improve the accuracy of the initial calculation and convergence speed of the accurate calculation.

The orbit period of ETO2 after the second impulse is applied is denoted by T_{tra2}, and then the semi-major axis a_{tra2} and the eccentricity e_{tra2} of ETO2 are expressed as

$$a_{tra2} = \left(\frac{\mu_m}{4\pi^2}T_{tra2}^2\right)^{\frac{1}{3}} \tag{23}$$

$$e_{tra2} = 1 - \frac{r_C}{a_{tra2}} \tag{24}$$

The third impulse vector is

$$\Delta \boldsymbol{v}_3 = \frac{\boldsymbol{h}_2 \times \boldsymbol{r}_C}{|\boldsymbol{h}_2 \times \boldsymbol{r}_C|}\sqrt{\frac{\mu_m}{r_C}}\left(\sqrt{1+e_{prl}} - \sqrt{2-\frac{r_C}{a_{tra2}}}\right) \quad (25)$$

Since the orbit planes are always changing under the influence of perturbation during the transfer between different planes, the intersection of LPO and ETO2 must be determined by interpolation. The orbit states of ETO2 and LPO at the time when the third impulse is applied are backward extrapolated for a period in the high-fidelity model, and the position and velocity vector of LPO and ETO2 at each moment can be obtained. The angle between the normal vector of the LPO plane and the position vector of ETO2 at each moment is

$$\theta(t) = \arccos(\boldsymbol{h}_1(t)\frac{\boldsymbol{r}_{tra2}(t)}{|\boldsymbol{r}_{tra2}(t)|}) \quad (26)$$

According to the change in the positive and negative values of the angle, the stopping condition of the extrapolation is determined, and the specific position of the intersection is further determined by interpolation. If the true anomaly f_B of the intersection on ETO2 is less than 90°, which indicates that the intersection is near the perilune of ETO2, it is necessary to continue the extrapolation until the intersection is near the apolune of ETO2. Hence, the orbit elements of ETO2 and LPO at the intersection can be obtained, and then the position vector $\boldsymbol{r}_B$ and the velocity vector $\boldsymbol{v}_{Btra2}$ of point B on ETO2 can be calculated.

The second impulse includes the component that changes the out-of-plane difference $\Delta \boldsymbol{v}_{21}$ and the component that changes the orbit in plane $\Delta \boldsymbol{v}_{22}$. The flight path angle κ and out-of-plane difference ξ are computed by

$$\kappa = \arctan\left(\frac{e_{tra2}\sin f_B}{1+e_{tra2}\cos f_B}\right) \quad (27)$$

$$\xi = \begin{cases} \arccos\left(\cos(\Omega_{tra2}-\Omega_A)\sin i_{tra2}\sin i_A \right. \\ \qquad \left. + \cos i_{tra2}\cos i_A\right), \quad u_{tra2} \geq 0 \\ -\arccos\left(\cos(\Omega_{tra2}-\Omega_A)\sin i_{tra2}\sin i_A \right. \\ \qquad \left. + \cos i_{tra2}\cos i_A\right), \quad u_{tra2} < 0 \end{cases} \quad (28)$$

where Ω_{tra2} and i_{tra2} are the right ascension of the ascending node and the orbit inclination of ETO2, respectively, and u_{tra2} is the argument of point B on ETO2.

Thus, in the selenocentric local vertical local horizon coordinate system of ETO2, $\Delta \boldsymbol{v}_{21}$ and $\Delta \boldsymbol{v}_{22}$ are respectively expressed as

$$\Delta \boldsymbol{v}_{21} = \begin{pmatrix} 0 \\ (1-\cos\xi)\cos\kappa \\ \sin\xi\cos\kappa \end{pmatrix} v_{Btra2} \quad (29)$$

$$\Delta \boldsymbol{v}_{22} = \begin{pmatrix} v_{Btra2}\sin\kappa \\ v_{Btra2}\cos\kappa\cos\xi - \sqrt{\dfrac{2\mu_m r_A}{r_B(r_B+r_A)}}\cos\xi \\ -v_{Btra2}\cos\kappa\sin\xi + \sqrt{\dfrac{2\mu_m r_A}{r_B(r_B+r_A)}}\sin\xi \end{pmatrix} \quad (30)$$

Hence, the second impulse vector is expressed as

$$\Delta \boldsymbol{v}_2 = \Delta \boldsymbol{v}_{21} + \Delta \boldsymbol{v}_{22} \quad (31)$$

The velocity vector of point B on ETO1 can be calculated by $\boldsymbol{r}_B$, $\boldsymbol{v}_{Btra2}$ and $\Delta \boldsymbol{v}_2$, and then the orbit elements can be obtained. In the ideal case, point B is the apolune of ETO1, and then the first impulse vector is

$$\Delta \boldsymbol{v}_1 = \frac{\boldsymbol{h}_1 \times \boldsymbol{r}_B}{|\boldsymbol{h}_1 \times \boldsymbol{r}_B|}\sqrt{\mu_m}\left(\sqrt{\frac{2r_B}{r_A(r_B+r_A)}} - \sqrt{\frac{1}{r_A}}\right) \quad (32)$$

2) FORWARD PATCHED-CONIC MODEL

The second and third segments are calculated by the patched-conic method. The semi-major axis of the selenocentric escape orbit is given by

$$a_{prl} = \frac{h_{prl}+r_m}{e_{prl}-1} \quad (33)$$

where r_m is the radius of the moon. The selenocentric perilune velocity can be expressed as

$$v_{prl} = \sqrt{\mu_m \frac{1+e_{prl}}{h_{prl}+r_m}} \quad (34)$$

Given i_{prl}, the perilune position vector and velocity vector in the perilune coordinate system are expressed as

$$\boldsymbol{r}_{prl} = \left(h_{prl}+r_m, 0, 0\right)^T \quad (35)$$

$$\boldsymbol{v}_{prl} = \left(0, v_{prl}\cos i_{prl}, v_{prl}\sin i_{prl}\right)^T \quad (36)$$

Given λ_{prl} and φ_{prl}, the perilune position vector and velocity vector in the selenocentric local vertical local horizon coordinate system are expressed as

$$\boldsymbol{r}_{prl}^{LVLH} = \boldsymbol{M}_3(-\lambda_{prl})\boldsymbol{M}_2(\varphi_{prl})\boldsymbol{r}_{prl} \quad (37)$$

$$\boldsymbol{v}_{prl}^{LVLH} = \boldsymbol{M}_3(-\lambda_{prl})\boldsymbol{M}_2(\varphi_{prl})\boldsymbol{v}_{prl} \quad (38)$$

where $\boldsymbol{M}_3(-\lambda_{prl})$ and $\boldsymbol{M}_2(\varphi_{prl})$ are the transition matrixes indicating rotating about the Z axis and Y axis through angles of $-\lambda_{prl}$ and φ_{prl}.

The perilune position vector and velocity vector in the selenocentric inertial coordinate system are obtained by

$$\boldsymbol{r}_{prl}^{MJ2} = \boldsymbol{M}_3(-\Omega_m)\boldsymbol{M}_1(-i_m)\boldsymbol{M}_3(-u_m)\boldsymbol{r}_{prl}^{LVLH} \quad (39)$$

$$\boldsymbol{v}_{prl}^{MJ2} = \boldsymbol{M}_3(-\Omega_m)\boldsymbol{M}_1(-i_m)\boldsymbol{M}_3(-u_m)\boldsymbol{v}_{prl}^{LVLH} \quad (40)$$

where Ω_m, i_m and u_m are the right ascension of the ascending node, the orbit inclination and the argument of the moon, respectively. The lunar orbit elements can be calculated by the Jet Propulsion Laboratory (JPL) ephemeris.

The transfer time of the second segment is calculated by

$$T_2 = \sqrt{\frac{a_{prl}^3}{\mu_m}}\left(e_{prl}\sinh H - H\right) \quad (41)$$

where H is the hyperbolic anomaly that can be obtained from the true anomaly f_{LSO} at point D:

$$\tan\frac{H}{2} = \sqrt{\frac{e_{prl}-1}{e_{prl}+1}}\tan\frac{f_{LSO}}{2} \quad (42)$$

Hence, the position vector and the velocity vector at point D in the selenocentric inertial coordinate system can

be obtained. The state vectors of point D in the geocentric inertial coordinate system can be acquired from the state vectors of the moon calculated by the JPL ephemeris, and the orbit elements can be transferred accordingly. The transfer time of the third segment is then expressed as

$$T_3 = \sqrt{\frac{a_{\mathrm{DE}}^3}{\mu_{\mathrm{e}}}}\left(E - \sinh E\right) \tag{43}$$

where μ_{e} is the gravitational parameters of Earth, a_{DE} is the semi-major axis of the geocentric return orbit, and E is the eccentric anomaly which can be calculated by the true anomaly f_{RE} of point E:

$$E = 2\arctan\left(\sqrt{\frac{1-e_{\mathrm{se}}}{1+e_{\mathrm{se}}}}\tan\frac{f_{\mathrm{RE}}}{2}\right) \tag{44}$$

f_{RE} is defined as

$$f_{\mathrm{RE}} = \begin{cases} 2\pi - \arccos\left(\dfrac{1}{e_{\mathrm{se}}}\left(\dfrac{r_{\mathrm{vcp}}}{r_{\mathrm{E}}}\left(1+e_{\mathrm{se}}\right)-1\right)\right), & r_{\mathrm{vcp}} \le r_{\mathrm{E}} \\ 2\pi, & r_{\mathrm{vcp}} > r_{\mathrm{E}} \end{cases} \tag{45}$$

where r_{vcp} and r_{E} are the radii of the vacuum perigee and the re-entry point, respectively. The position vector and the velocity vector of the re-entry point can then be acquired. The longitude and latitude of the re-entry point can be obtained from the orbit elements of the re-entry point. The departure time is adjusted to satisfy the constraint of the longitude of the re-entry point. Then, the range angle is adjusted to satisfy the constraint of the latitude of the re-entry point. By this method, the location of the landing site with a higher accuracy can be obtained.

In the initial calculation, the sequential quadratic programming sparse nonlinear optimizer (SQP_SNOPT) algorithm is adopted to generate the initial orbit. To improve the convergence speed, the equality constraints are set to the objective function [32]:

$$J_{\mathrm{I}} = \left|i' - i_{\mathrm{se}}\right| + \psi\left|h' - h_{\mathrm{vcp}}\right| + \left|\lambda' - \lambda_{\mathrm{rp}}\right| + \left|\phi' - \phi_{\mathrm{rp}}\right| \tag{46}$$

where ψ is the relative weight factor, which is calculated according to the angle and distance unit, combined with the magnitude of Earth's radius. i', h', λ' and ϕ' are the variation values of the geocentric return orbit inclination, the vacuum perigee altitude, and the longitude and latitude of the re-entry point in the iteration process, respectively.

C. ACCURATE DESIGN

In the accurate design, the return orbit is divided into two segments: the three-impulse maneuver segment and the lunar escape segment. The backward and forward integral calculations are performed in the high-fidelity model. The SQP_SNOPT algorithm is used to optimize the two segments.

In the geocentric J2000 coordinate system, considering the relevant perturbation factors, the accurate force model is expressed as

$$\frac{\mathrm{d}^2\boldsymbol{R}}{\mathrm{d}t} = -\frac{\mu_{\mathrm{e}}\boldsymbol{R}}{R^3} + \boldsymbol{A}_{\mathrm{N}} + \boldsymbol{A}_{\mathrm{NSE}} + \boldsymbol{A}_{\mathrm{NSM}} + \boldsymbol{A}_{\mathrm{R}} + \boldsymbol{A}_{\mathrm{D}} + \boldsymbol{A}_{\mathrm{P}} \tag{47}$$

where $\boldsymbol{R}$ is the position vector with respect to the geocentric J2000 coordinate system; $\boldsymbol{A}_{\mathrm{N}}$ is the gravitation perturbation of the N-body, where only the solar and lunar perturbations are considered and the relative positions between the stars are obtained by JPL ephemeris; $\boldsymbol{A}_{\mathrm{NSE}}$ is the Earth's non-spherical perturbation; $\boldsymbol{A}_{\mathrm{NSM}}$ is the Moon's non-spherical perturbation; $\boldsymbol{A}_{\mathrm{R}}$ is the solar pressure perturbation; $\boldsymbol{A}_{\mathrm{D}}$ is the atmospheric drag perturbation; and, $\boldsymbol{A}_{\mathrm{P}}$ is the thrust acceleration. The perturbation of Jupiter, Venus and other large planets, Earth's tides, and the relativistic effect are ignored.

Regarding the LEO segment, the initial design result serves as the initial value in the high-fidelity model, with the optimization objective and constraint conditions consistent with the initial design.

For the three-impulse maneuver segment, the following parameters are selected as optimization variables: the first impulse vector $\Delta\boldsymbol{v}_1$, the second impulse vector $\Delta\boldsymbol{v}_2$, the third impulse vector $\Delta\boldsymbol{v}_3$, and the time interval of the first two impulses T_{12}. The orbit elements of the departure point can be obtained by backward extrapolation in the high-fidelity model. The constraint conditions are expressed as

$$\begin{cases} i_{\mathrm{HP}} = i_{\mathrm{A}} \\ \Omega_{\mathrm{HP}} = \Omega_{\mathrm{A}} \\ e_{\mathrm{HP}} = 0 \\ h_{\mathrm{HP}} = h_{\mathrm{A}} \end{cases} \tag{48}$$

where i_{HP}, Ω_{HP}, e_{HP}, and h_{HP} are the orbit inclination, the right ascension of the ascending node, the eccentricity and the orbit height of the circumlunar orbit obtained by backward high-fidelity extrapolation, respectively.

The objective of optimization is to minimize the sum of three impulse magnitudes:

$$J = \min(\Delta v_1 + \Delta v_2 + \Delta v_3) \tag{49}$$

In conclusion, the flow chart of the orbit design strategy is shown as Fig. 10.

V. SIMULATION VERIFICATION AND ANALYSIS

This section is devoted to numerical simulations to verify the feasibility and validity of the orbit design strategy proposed in the previous section, and to analyze the related characteristics of the return orbit.

A. SIMULATION VERIFICATION

The parameters of the simulation example are set as follows: in the moon's fixed coordinate system, the longitude of the ascending node, the height, the inclination and the eccentricity of the LPO are 70°, 300 km, 90° and 0, respectively. The perilune time is searched between 2028-01-18 and 2028-01-19. The LEO perilune altitude is 200 km, and the period of ETO2 is 21.6 h. The geocentric return orbit inclination is 43°, the maximum range angle is 70°, and

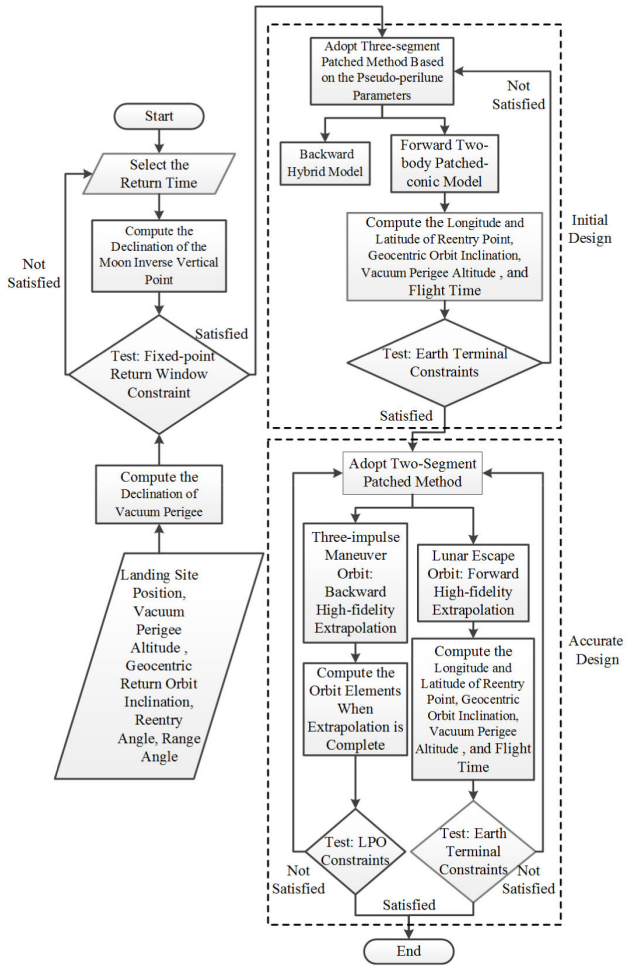

FIGURE 10. The flow chart of the orbit design strategy.

the vacuum perigee altitude is 51 km. The location of the landing point is (100°E, 41°N), and the maximum flight time is 3.5 days.

To verify the feasibility of the proposed fixed-point return method and highlight its characteristic, a comparison between it and the existing method in the reference is firstly given. Owing to the decoupling of the three-impulse maneuver and the lunar escape, the comparison is performed for the lunar escape segment. According to the parameters setting, the proposed method is adopted to generate the fixed-point return orbit. At the same time, the fixed-point return method in the reference [23] is adopted to solve the same problem. The results are shown in Table 1.

As shown in Table 1, the proposed method in this paper has a little higher accuracy. However, compared to the method in the reference [23], the calculation time of the proposed method in this paper is obviously shorter. Thus, the proposed method has a higher efficiency of calculation than the method in the reference.

Then, the results of the initial design and the accurate design by this strategy are depicted in Table 2. The three impulse vectors are described in the moon J2000 coordinate system.

TABLE 1. The results of different methods.

Orbit Parameter	Method in this Paper	Method in the Reference [23]
Perilune Time	2028-01-18 16: 12: 06	2028-01-18 16: 10: 27
h_{prl}	200 km	200 km
T (day)	2.07	2.08
λ_{rp}	45.35°	45.36°
ϕ_{rp}	13.48°	13.49°
h_{vcp}	51.00 km	50.99 km
i_{se}	43.00°	42.99°
Calculation Time (s)	0.6	25

TABLE 2. The results of the orbit design.

Orbit Parameter	Initial Design	Accurate Design
$\Delta \boldsymbol{v}_1$ time	2028-01-17 18: 06: 07	2028-01-17 19: 40: 39
$\Delta \boldsymbol{v}_1$ (m/s)	(-129.69, 477.73, -193.68)	(137.42, 486.61, -163.48)
$\Delta \boldsymbol{v}_2$ time	2028-01-18 04: 50: 27	2028-01-18 06: 06: 22
$\Delta \boldsymbol{v}_2$ (m/s)	(21.37, 4.21, 27.65)	(15.36, -10.99, -19.91)
$\Delta \boldsymbol{v}_3$ time	2028-01-18 16: 12: 06	2028-01-18 16: 12: 06
$\Delta \boldsymbol{v}_3$ (m/s)	(63.66, 341.05, -117.42)	(59.19, 356.99, -117.70)
Total Velocity Increment (m/s)	933.03	939.38
T (day)	2.92	2.91
h_{prl}	200 km	200 km
e_{prl}	1.46	1.48
i_{prl}	260.12°	259.06°
φ_{prl}	-43.82°	-44.33°
λ_{prl}	40.06°	40.26°

As shown in Table 2, the results of the initial design and accurate design have small differences. In the simulation process, the result of the accurate design can converge quickly by taking the result of the initial design as the initial value of the accurate design. The accurate orbit in space is shown in Fig. 11.

B. ORBIT CHARACTERISTIC ANALYSIS

In the orbit scheme design stage, more attention is paid to the rules and characteristics of a class of orbits in terms of engineering, but less attention is paid to the design of one specific orbit. Because of the advantages of high precision and good convergence, the serial design strategy proposed in the previous section is applied in this subsection. Based on a large number of simulations, the characteristic analysis of the three-impulse return orbit is discussed.

1) FIXED-POINT RETURN WINDOW CHARACTERISTIC

For manned lunar missions, successfully returning to the intended landing site is an important task and a basic requirement of the missions. The analysis of the fixed-point return

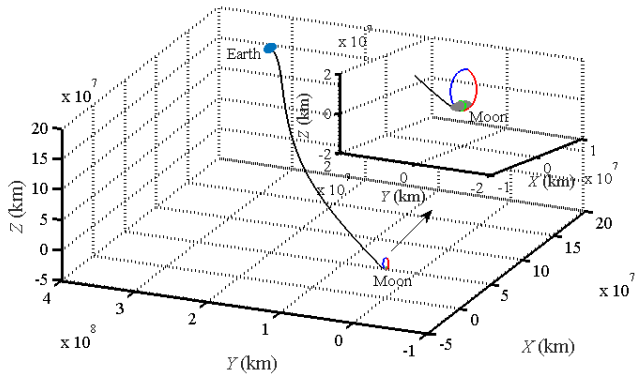

FIGURE 11. Accurate orbit in space.

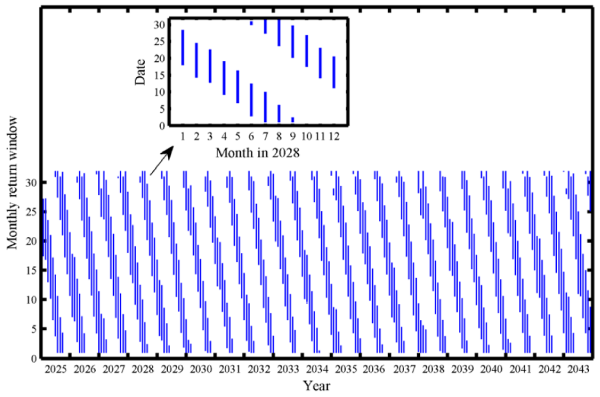

FIGURE 12. Monthly fixed-point return window in 2025-2043.

window is of great significance to the return orbit design and the selection of the mission implementation time. The range angle in the re-entry process is set to 45°-70°, the geocentric return orbit inclination is 43°, the vacuum perigee altitude is 51 km, and the location of the landing point is (100°E, 41°N). It is known that the variation period of the declination of the moon is 18.6 years. Fig. 12 depicts the monthly fixed-point return window for 19 years from 2025 to 2043. It is noted that the monthly return window displays a periodic change of approximately nine months as a whole, but there are some differences in each period. Assuming that the manned lunar mission will be carried out in 2028, the monthly fixed-point return window in 2028 is shown at the top of Fig. 12. As shown in the partial enlargement figure, the fixed-point return window in each month from June to September has two phases, both longer than 10.5 days. Among them, the fixed-point return window of July is the longest, which is over 13.5 days. All other months have one fixed-point return window of approximately 10 days.

Taking January 2028 as an example, the influence on the fixed-point return window by i_{se} and the latitude of landing site ϕ_L are analyzed. i_{se} is varied while holding the other parameters constant, and the fixed-point return window is calculated. As illustrated in Fig. 13, the fixed-point return window increases with increasing of i_{se}. The relationship between ϕ_L and the fixed-point return window is shown

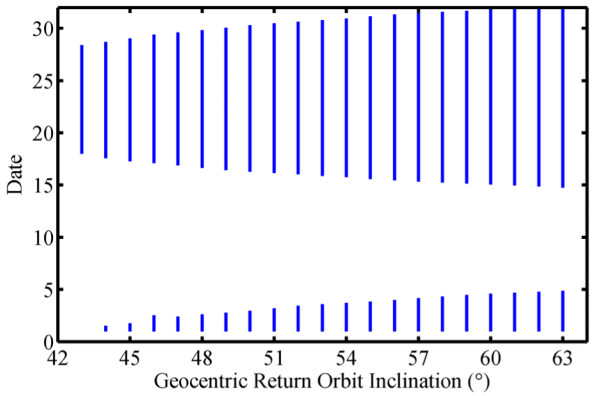

FIGURE 13. Fixed-point return window versus geocentric return orbit inclination.

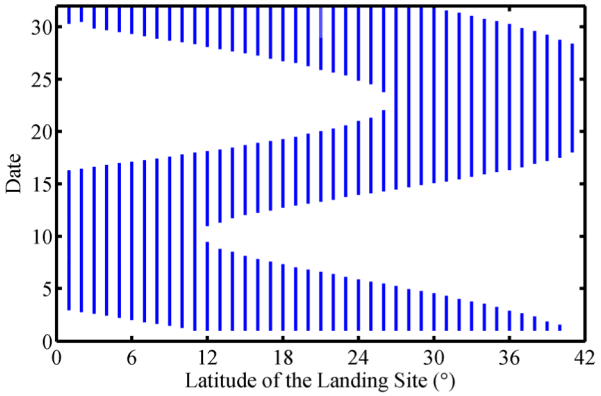

FIGURE 14. Fixed-point return window versus the latitude of the landing site.

in Fig. 14. An interesting finding is that the whole figure is nearly centrosymmetrical about the point (19°N, January 19). The landing site is between 12°N and 26°N; there are three return windows in January and only two return windows at other latitudes. The number of fixed-point return days corresponding to different latitudes of the landing site is displayed in Fig. 15. It can be observed that when the landing site is between the equator and 11°N, the number of fixed-point return days grows gradually with increasing ϕ_L, and vice versa between 27°N and 41°N. In addition, a small change in the range of fixed-point return days occurs between 12°N and 26°N.

Therefore, from the perspective of the security of the mission implementation, it is necessary to ensure that the fixed-point return window is as long as possible. From 2025 to 2043, the fixed-point return window is longer in 2026 and 2043. With ϕ_L fixed, i_{se} can be set as large as possible. When i_{se} is 43°, the landing site can be set at 27°N.

2) VELOCITY INCREMENT CHARACTERISTIC

Another indicator necessary for engineering is the velocity increment consumption. The parameters in the simulation example are set as follows: in the moon fixed coordinate system, the height, the orbit inclination and the eccentricity of the LPO are 200 km, 90° and 0, respectively. The period

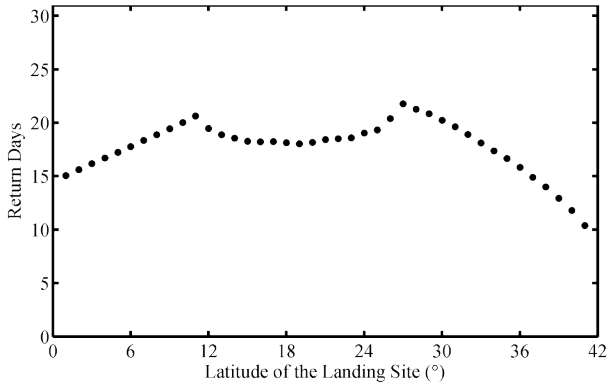

FIGURE 15. Fixed-point return days versus the latitude of the landing site.

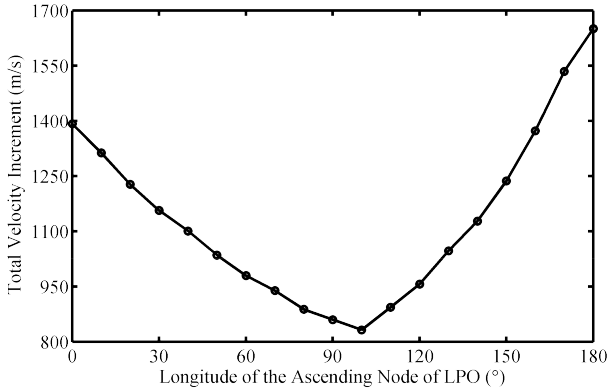

FIGURE 16. Total velocity increment versus the longitude of the ascending node of LPO.

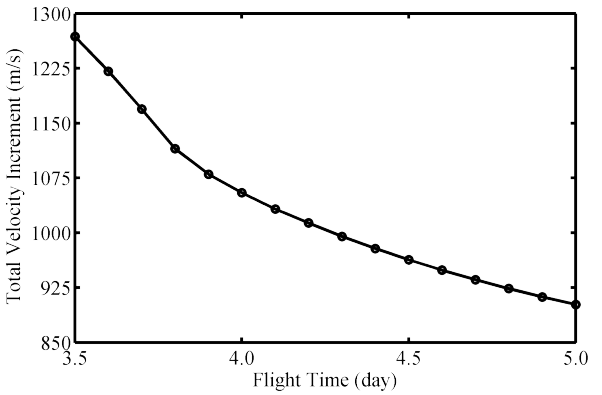

FIGURE 17. Total velocity increment versus flight time.

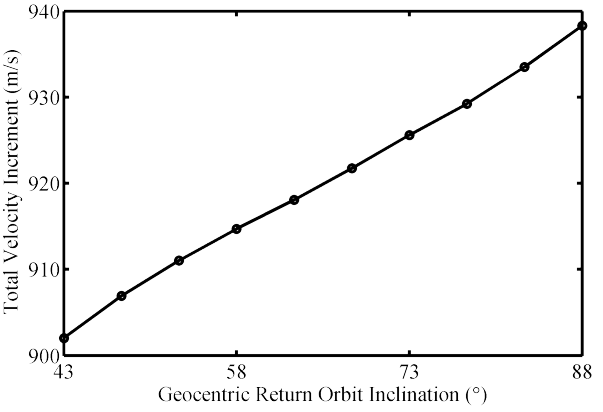

FIGURE 18. Total velocity increment versus the geocentric return orbit inclination.

of ETO2 is 24 h. The perilune time is searched between 2028-01-18 and 2028-01-19. The perilune altitude is 200 km, the geocentric return orbit inclination is 43°, the range angle is 70°, and the vacuum perigee altitude is 51 km. The position of the landing site is (100°E, 41°N), and the maximum flight time is 5 days. The variation of Δv for the range in the longitude of the ascending node of LPO from 0° to 180° is depicted in Fig. 16. A noticeable characteristic of the curve is that when the longitude of the ascending node is 100°, Δv achieves a minimum of approximately 830 m/s, while Δv achieves a maximum of approximately 1650 m/s when the longitude of the ascending node is 180°. It can be concluded that when the direction of the connection between the ascending node and the descending node of LPO is nearly vertical to the direction of the moon-Earth connection, the impulse consumption is small and can be selected as the optimal departure position, while the impulse consumption is large when the direction of the connection between the ascending node and the descending node of LPO is close to the direction of the Moon-Earth connection. The above variation rule is consistent with the results obtained by the indirect method in [33], but the impulse consumption is relatively large due to the consideration of the constraint of the landing site in this paper. In addition, the result of numerical optimization is compared with that of the preliminary analysis using the convenient method described in Sect. 3. The difference in magnitude between them is small, which proves the correctness of the result. However, because Earth's terminal constraints are considered, the numerical result is slightly larger than that of the preliminary analysis.

Given the longitude of the ascending node of LPO as 111.25°, the effect of T on Δv is analyzed. It is clear that Δv decreases with increasing T from Fig. 17. This characteristic is consistent with the conclusion obtained by the indirect method in [33]. As observed in Fig. 18, Δv is plotted as a function of i_{se}. When i_{se} increases from 43° to 88°, Δv has a slight increase by approximately 40 m/s. It is noted from Fig. 19 that Δv is decreases with increasing h_{prl}, but the change in the magnitude is small.

Therefore, from the perspective of engineering application, it is essential to guarantee that the velocity increment consumption is as small as possible. A three-impulse maneuver can be started from LPO, in which the direction of the connection between the ascending node and the descending node is close to the vertical direction of the moon-Earth connection, and an LEO with a higher perilune altitude can be selected to return to the Earth landing site with a smaller geocentric return orbit inclination. On the premise of ensuring astronaut safety, the flight time can be as long as possible.

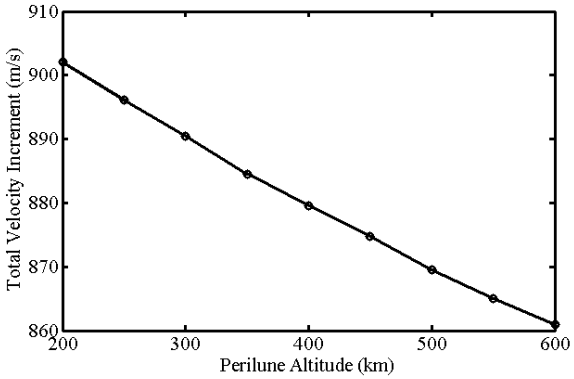

FIGURE 19. Total velocity increment versus the perilune altitude.

VI. CONCLUSION

Aiming at manned lunar return missions intended for high-latitude regions, a return orbit scheme of the three-impulse maneuver is studied. A convenient method is proposed for the preliminary analysis of the velocity increment, which is based on the conical surface of the hyperbolic excess velocity and uses the angular coupling relationship of the related vectors in space. A serial orbit design strategy from the initial calculation to the accurate calculation is employed, considering the constraint of the Earth landing site. In the initial design, a three-segment orbit patched method based on the pseudo-perilune parameters is adopted to generate the initial value. In accurate design, a two-segment orbit patched method is applied in the high-fidelity model. The effectiveness and feasibility of the strategy are examined by numerical simulation, and the fixed-point return window and the velocity increment characteristics are further analyzed by the sum of the simulation calculations. The research results are summarized as follows:

1). The results of the convenient method for preliminary analysis of the velocity increment indicate that the maximum Δv required for this orbit scheme is approximately 1600 m/s, and the minimum Δv is less than 900 m/s. Targeting a smaller $\boldsymbol{v}_{\infty \text{out}}$ and selecting the ETO of a longer period for the maneuver are both beneficial in reducing the velocity increment consumption.

2). The results of the fixed-point return window characteristic analysis show that the monthly fixed-point return window changes periodically approximately every nine months.

3). Considering the lower velocity increment, the three-impulse maneuver can be started from LPO, in which the direction of the connection between the ascending node and the descending node is nearly vertical to the moon-Earth connection, and an LEO with higher perilune altitude can be selected to return. The flight time can be longer to ensure astronaut safety.

4). The increase in the geocentric return orbit inclination is conducive to expanding the fixed-point return window, but also increases the consumption of the velocity increment. Hence, the selection of the geocentric return orbit inclination must be considered comprehensively.

In summary, this paper designs and analyzes the three-impulse return orbit scheme for manned lunar missions and the research conclusions can provide a valuable reference for them.

REFERENCES

[1] E. Sim, "Current development trends in lunar explorers around the world," *Aeronaut. Space Sci.*, vol. 44, no. 8, pp. 741–757, 2016.

[2] J. Foust, "Gateway or bust: NASA's plan for a 2024 lunar landing depends on a much-criticized orbital outpost," *IEEE Spectr.*, vol. 56, no. 7, pp. 32–37, Jul. 2019, doi: 10.1109/MSPEC.2019.8747310.

[3] A. Zak, "Russia shoots for the moon," *Aerosp. Amer.*, vol. 53, no. 3, pp. 26–31, 2015.

[4] S. C. Aleina, N. Viola, R. Fusaro, G. Saccoccia, and V. Vercella, "Using the ESA exploration technology roadmaps in support of new mission concepts and technology prioritization," *Acta Astronautica*, vol. 154, pp. 170–176, Jan. 2019, doi: 10.1016/j.actaastro.2018.04.035.

[5] K. J. Kim, "A research trend on lunar resources and lunar base," *J. Petrol. Soc. Korea*, vol. 26, no. 4, pp. 373–384, 2017, doi: 10.7854/JPSK.2017.26.4.373.

[6] W. Wu, C. Li, W. Zuo, H. Zhang, J. Liu, W. Wen, Y. Su, X. Ren, J. Yan, D. Yu, G. Dong, C. Wang, Z. Sun, E. Liu, J. Yang, and Z. Ouyang, "Lunar farside to be explored by Chang'e-4," *Nature Geosci.*, vol. 12, no. 4, pp. 222–223, Mar. 2019, doi: 10.1038/s41561-019-0341-7.

[7] Y. Jia, Y. Zou, J. Ping, C. Xue, J. Yan, and Y. Ning, "The scientific objectives and payloads of Chang'e-4 mission," *Planet. Space Sci.*, vol. 162, pp. 207–215, Nov. 2018, doi: 10.1016/j.pss.2018.02.011.

[8] C. Li, C. Wang, Y. Wei, and Y. Lin, "China's present and future lunar exploration program," *Science*, vol. 365, no. 6450, pp. 238–239, Jul. 2019, doi: 10.1126/science.aax9908.

[9] S. Li, P. G. Lucey, R. E. Milliken, P. O. Hayne, E. Fisher, J.-P. Williams, D. M. Hurley, and R. C. Elphic, "Direct evidence of surface exposed water ice in the lunar polar regions," *Proc. Nat. Acad. Sci. USA*, vol. 115, no. 36, pp. 8907–8912, Aug. 2018, doi: 10.1073/pnas.1802345115.

[10] C. Zhu, P. B. Crandall, J. J. Gillis-Davis, H. A. Ishii, J. P. Bradley, L. M. Corley, and R. I. Kaiser, "Untangling the formation and liberation of water in the lunar regolith," *Proc. Nat. Acad. Sci. USA*, vol. 116, no. 23, pp. 11165–11170, Jun. 2019, doi: 10.1073/pnas.1819600116.

[11] M. V. Djachkova, M. L. Litvak, I. G. Mitrofanov, and A. B. Sanin, "Selection of luna-25 landing sites in the south polar region of the moon," *Sol. Syst. Res.*, vol. 51, no. 3, pp. 185–195, May 2017, doi: 10.1134/S0038094617030029.

[12] S. Y. Yim and H. Baoyin, "High-latitude-landing circumlunar free return trajectory design," *Aircr. Eng. Aerosp. Technol.*, vol. 87, no. 4, pp. 380–391, Jul. 2015, doi: 10.1108/AEAT-05-2013-0092.

[13] P. D. Wooster, "Strategies for affordable human moon and mars exploration," M.S. thesis, Dept. Aeronaut. Aeronaut., Massachusetts Inst. Technol., Cambridge, MA, USA, 2007.

[14] D. R. Jones and C. Ocampo, "Optimization of impulsive trajectories from a circular orbit to an excess velocity vector," *J. Guid., Control, Dyn.*, vol. 35, no. 1, pp. 234–244, Jan. 2012, doi: 10.2514/1.52527.

[15] Z. S. Wang *et al.*, "Optimization design of spacecraft trans-earth insertion strategy," *Spacecr. Eng.*, vol. 28, no. 1, pp. 10–18, 2019.

[16] C. Ocampo and R. R. Saudemont, "Initial trajectory model for a multi-maneuver moon-to-earth abort sequence," *J. Guid., Control, Dyn.*, vol. 33, no. 4, pp. 1184–1194, Jul. 2010, doi: 10.2514/1.46955.

[17] J. Li, S. Gong, and X. Wang, "Analytical design methods for determining moon-to-earth trajectories," *Aerosp. Sci. Technol.*, vol. 40, pp. 138–149, Jan. 2015, doi: 10.1016/j.ast.2014.10.016.

[18] T. N. Edelbaum, "Optimal nonplanar escape from circular orbits," *AIAA J.*, vol. 9, no. 12, pp. 2432–2436, Dec. 1971, doi: 10.2514/3.50047.

[19] A. W. Zheng and J. P. Zhou, "A search strategy of back windows for moon-to-earth trajectories directly returning to the earth," *Acta Aeronautica et Astronautica Sinica*, vol. 35, no. 8, pp. 2243–2250, Aug. 2014, doi: 10.7527/S1000-6893.2014.0085.

[20] N. M. Gavrikova and Y. F. Golubev, "Construction of the return trajectory from the lunar parking orbit to the earth's atmosphere reentry point," *Keldysh Inst. Preprints*, no. 53, pp. 1–39, 2019, doi: 10.20948/prepr-2019-53.

[21] C. Park, Q. Gong, I. Ross, and P. Sekhavat, "Fuel optimal design of moon-earth trajectories using legendre pseudospectral method," in *Proc. AIAA/AAS Astrodyn. Spec. Conf. Exihib.*, Honolulu, HI, USA, 2008, pp. 1–15.
[22] L. Yue, W.-X. Jing, and Y.-Y. Xiao, "Finite thrust transfer strategy designing for low energy moon return based on GPM/VSM," *Int. J. Autom. Comput.*, vol. 12, no. 5, pp. 490–496, Aug. 2015, doi: 10.1007/s11633-014-0869-3.
[23] H. Shen, J. Zhou, Q. Peng, and H. Li, "Point return orbit design and characteristics analysis for manned lunar mission," *Sci. China Technol. Sci.*, vol. 55, no. 9, pp. 2561–2569, Sep. 2012.
[24] B. He, H. Li, H. Shen, and Q. Peng, "Coupled design of landing window and point return orbit for manned lunar landing mission," *J. Nat. Univ. Defense Technol.*, vol. 39, no. 1, pp. 11–16, Feb. 2017, doi: 10.11887/j.cn.201701003.
[25] M. J. Chung and S. S. Weinstein, "Trajectory design of lunar south pole-Aitken basin sample return mission," in *Proc. AIAA/AAS Astrodyn. Spec. Conf. Exihib.*, Providence, RI, USA, 2004, pp. 1–10.
[26] J. S. Parker, T. P. McElrath, R. L. Anderson, and T. H. Sweetser, "Trajectory design for MoonRise: A proposed lunar south pole aitken basin sample return mission," *J. Astron. Sci.*, vol. 62, no. 1, pp. 44–72, Jun. 2015, doi: 10.1007/s40295-015-0037-1.
[27] F. Feng and Y. S. Zhang, "Application and analysis of an improved multiconic method in trajectory design of the lunar south pole return mission," *J. Aerosp. Eng.*, vol. 232, no. 6, pp. 1063–1076, Apr. 2017, doi: 10.1177/0954410017705896.
[28] B. Y. He, "Analysis approaches for precision reachable sets of manned lunar orbits using numerical continuation theory," Ph.D. dissertation, College Aerosp. Space Sci., Nat. Univ. Defense Technol., Changsha, China, 2017.
[29] Q. B. Peng, "Optimal trajectory design and characteristics analysis for manned lunar landing mission with emergency return capability," Ph.D. dissertation, College Aerosp. Space Sci., Nat. Univ. Defense Technol., Changsha, China, 2011.
[30] H. X. Shen, "Optimization of method for the moon-earth abort return trajectories based on analytical homotopic technology," Ph.D. dissertation, Dept. College Aerosp. Space Sci., Nat. Univ. Defense Technol., Changsha, China, 2014.
[31] W. Zhou, H. Li, B. He, L. Yang, and Q. Peng, "Fixed-thrust earth-moon free return orbit design based on a hybrid multi-conic method of pseudo-perilune parameters," *Acta Astronautica*, vol. 160, pp. 365–377, Jul. 2019, doi: 10.1016/j.actaastro.2019.04.034.
[32] B. Y. He, H. Y. Li, and J. P. Zhou, "Rapid design of circumlunar free return high accuracy trajectory and trans-lunar window for manned lunar landing mission," *J. Astronaut.*, vol. 37, no. 5, pp. 518–521, May 2016.
[33] H.-X. Shen and L. Casalino, "Indirect optimization of three-dimensional multiple-impulse moon-to-earth transfers," *J. Astron. Sci.*, vol. 61, no. 3, pp. 255–274, Nov. 2014, doi: 10.1007/s40295-014-0018-9.

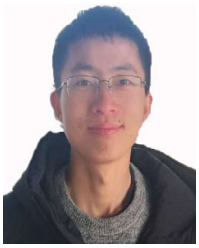

LIN LU received the B.E. degree from the College of Aerospace Science and Engineering, National University of Defense Technology, where he is currently pursuing the M.E. degree. His research interests include orbit design and optimization for the manned lunar missions.

HAIYANG LI received the B.E., M.E., and Ph.D. degrees from the College of Aerospace Science and Engineering, National University of Defense Technology. He is currently a Professor with the College of Aerospace Science and Engineering, National University of Defense Technology. His research interest includes aerospace system simulation and analysis.